Published in final edited form as:
Cancer Res. 2014 September 1; 74(17): 4638–4652. doi:10.1158/0008-5472.CAN-13-3534.

Diffusion-weighted imaging in cancer: Physical foundations and applications of Restriction Spectrum Imaging

Nathan S. White[1,*], **Carrie McDonald**[2], **Niky Farid**[1], **Josh Kuperman**[1], **David Karow**[1], **Natalie M. Schenker-Ahmed**[1], **Hauke Bartsch**[1], **Rebecca Rakow-Penner**[1], **Dominic Holland**[1], **Ahmed Shabaik**[7], **Atle Bjørnerud**[8], **Tuva Hope**[9], **Jona Hattangadi-Gluth**[4], **Michael Liss**[5], **J. Kellogg Parsons**[5], **Clark C. Chen**[6], **Steve Raman**[10], **Daniel Margolis**[10], **Robert E. Reiter**[11], **Leonard Marks**[11], **Santosh Kesari**[3], **Arno J. Mundt**[4], **Chris J. Kane**[5], **Bob S. Carter**[6], **William G. Bradley**[1], and **Anders M. Dale**[1,3]

[1]Department of Radiology, University of California, San Diego

[2]Department of Psychiatry, University of California, San Diego

[3]Department of Neurosciences, University of California, San Diego

[4]Department of Radiation Oncology, University of California, San Diego

[5]Department of Urology, University of California, San Diego

[6]Center for Theoretical and Applied Neuro-Oncology, Division of Neurosurgery, University of California, San Diego

[7]Department of Pathology, University of California, San Diego

[8]Department of Physics, University of Oslo, Oslo, Norway

[9]Department of Circulation and Medical Imaging, Norwegian University of Science and Technology, Trondheim, Norway

[10]Department of Radiology, University of California, Los Angeles

[11]Department of Urology, University of California, Los Angeles

Abstract

Diffusion weighted imaging (DWI) has been at the forefront of cancer imaging since the early 2000's. Prior to its application in clinical oncology, this powerful technique had already achieved widespread recognition due to its utility in the diagnosis of cerebral infarction. Following this initial success, the ability of DWI to detect inherent tissue contrast began to be exploited in the field of oncology. Although the initial oncologic applications for tumor detection and characterization, assessing treatment response, and predicting survival were primarily in the field of neuro-oncology, the scope of DWI has since broadened to include oncologic imaging of the

Address for correspondence: N. S. White, Multimodal Imaging Laboratory, Suite C101; 8950 Villa La Jolla Drive, La Jolla, CA 92037; phone: 858-534-2678; fax: 858-534-1078; nswhite@ucsd.edu.

Conflicts of interest: None of the authors have any personal or institutional financial interest in drugs, materials, or devices described in this submission.

prostate gland, breast, and liver. Despite its growing success and application, misconceptions as to the underlying physical basis of the DWI signal exist among researchers and clinicians alike.

In this review, we provide a detailed explanation of the biophysical basis of diffusion contrast, emphasizing the difference between hindered and restricted diffusion, and elucidating how diffusion parameters in tissue are derived from the measurements via the diffusion model. We describe one advanced DWI modeling technique, called Restriction Spectrum Imaging (RSI). This technique offers a more direct *in vivo* measure of tumor cells, due to its ability to distinguish separable pools of water within tissue based on their intrinsic diffusion characteristics. Using RSI as an example, we then highlight the ability of advanced DWI techniques to address key clinical challenges in neuro-oncology, including improved tumor conspicuity, distinguishing actual response to therapy from pseudoresponse, and delineation of white matter tracts in regions of peritumoral edema. We also discuss how RSI, combined with new methods for correction of spatial distortions inherent diffusion MRI scans, may enable more precise spatial targeting of lesions, with implications for radiation oncology, and surgical planning.

INTRODUCTION

Diffusion-weighted imaging (DWI) is increasingly used as an imaging biomarker for the detection and characterization of primary and metastatic brain tumors as well as for prognostication and monitoring treatment response in this patient population. The unique ability of this technique to probe the underlying structure of brain tissue at a cellular level makes it well poised to answer questions regarding tumor biology, as well as the microstructure of peritumoral white matter. The greatest enthusiasm to date has surrounded the ability of DWI to estimate tumor cellularity on the basis of quantitative images of diffusion, namely apparent diffusion coefficient (ADC) maps. In particular, numerous investigators have shown a negative correlation between tumor ADC values and cellularity (1–3), which is commonly attributed to increased *restricted* diffusion imposed by tumor cells. Following this logic, ADC has been used with varying success to characterize and grade primary and metastatic brain tumors (3–9), to assess tumor response to therapy (10–12), and to predict survival in patients with malignant tumors (13–17). However, confusion as to the true biophysical basis of the DWI signal abounds, and awareness of the limitations of the existing approaches has led to the development of advanced DWI methods that extend beyond the tensor model. These methods include high-angular diffusion imaging techniques, such as diffusion spectrum imaging (DSI) (18) and Q-ball imaging (19), as well as methods to probe non-Gaussian diffusion, including biexponential (20, 21), stretched exponential (22), and kurtosis imaging (23), and methods to study perfusion-related effects at low b-values, such as intravoxel incoherent motion (IVIM) (24). While these techniques often provide a better characterization of tissue architecture than traditional models, the relationship of these measures to the underlying pathophysiology of tumors is largely unknown.

Advances in MR technology are now creating even more possibilities, increasing excitement in the field by broadening the potential applications of DWI within cancer diagnosis and treatment. Newer scanners with improved gradient performance allow for higher b-values with shorter diffusion- and echo times. In addition, improved coil technology and higher

field strength provide better signal-to-noise ratio (SNR). With these MR advancements, it has become possible to develop new, innovative DWI methods that provide more direct measures of tumor cellularity by leveraging the intrinsic contrast of tumor cells relative to other tissues. Such direct measures address a top challenge posed by the NCI to develop *in vivo* imaging methods that portray tumor "cytotypes," i.e., imaging methods that can *probe the identity, quantity, and location of different cells that make up a tumor and its microenvironment* [NIH RFA-CA-13-020]. However, the successful application of such methods requires not only advanced MR technology and an appreciation of the clinical challenges in neuro-oncology, but also an exquisite understanding of the physical basis of the DWI signal and its current limitations.

The purpose of this review is to provide a detailed explanation of the biophysical basis of diffusion contrast and to demonstrate what is known about how it reflects tissue microstructure in the context of key clinical dilemmas in neuro-oncology. We begin with a basic introduction of how diffusion measurements are derived from DWI and then follow with a review of the biophysical properties of water diffusion in tissue. We then describe how diffusion parameters in tissue are derived from the measurements via fitting of the diffusion model to observed data. For this review, we focus on one advanced DWI modeling technique called *Restriction Spectrum Imaging (RSI*), which provides a general framework for estimating tissue properties from DWI data and addresses the NCI challenge for more direct, *in vivo* imaging of tumor cells. We also address the power of multispectral imaging, highlighting the importance of combining advanced DWI methods such as RSI with other imaging modalities (i.e., MRI perfusion, PET) in order to optimize the detection and monitoring of brain tumors. Although the primary focus this review is on the application of RSI to neuro-oncology, the same methods are equally applicable to other applications of oncologic imaging, such as prostate, liver, and breast cancer, and we briefly present some preliminary data in prostate cancer at the end of the clinical applications section.

PRINCIPLES OF DIFFUSION MRI

The diffusion experiment

While early diffusion measurements using nuclear magnetic resonance (NMR) in biological tissue were made in the 1960s and 1970s, it was not until the mid 1980s that the basic principles of DWI emerged (25–27). All MRI techniques including DWI rely on the fundamental principle that water hydrogen nuclei become magnetized when placed in a strong static magnetic field. MRI contrast is formed by perturbing this magnetization using electromagnetic waves and then allowing the magnetization to "relax" back to an equilibrium state. Tissue relaxation times - namely the spin-lattice (T_1) and spin-spin (T_2) relaxation times - form the fundamental basis of soft tissue contrast and anatomical imaging with MRI. DWI is an MRI technique that adds additional sensitivity to the intrinsic random thermal displacements of water molecules that take place during the MRI experiment as part of the natural diffusion process. A pair of pulsed magnetic field gradients are turned on and off in succession (with duration δ) to magnetically "label" and "refocus" the spin phase of hydrogen nuclei depending on where they reside physically in the gradient field (Fig 1). The second refocusing pulse is applied some finite time Δ after the first pulse in an effort to

realign the spin phases of stationary nuclei. Thus, any residual spin phase left after the application of the refocusing pulse can be attributed to the diffusion of water along the orientation of the field gradient during the effective diffusion time of the experiment T_d, defined here as Δ-(δ/3). The net phase dispersion due to diffusion causes an attenuation of the measured signal and a decrease in the voxel intensity. Stejkal and Tanner (28) were some of the pioneers of the pulsed field gradient experiment and provided the mathematic framework to relate the diffusion coefficient to the experimental variables. To date, the Stejkal Tanner pulse sequence remains the gold standard method for measuring diffusion in the clinic and forms the basis of quantitative mapping of tumor cellularity with the apparent diffusion coefficient (ADC), as discussed below.

Biophysics of water diffusion in tissue

In this section we provide a basic review of the three principal physical modes of diffusion in tissue: free, hindered, and restricted.

Free diffusion—Free water diffusion describes the random (Brownian) motion of water molecules due to thermal agitation, in the absence of any obstacles. The displacement distribution of free water molecules is time dependent and Gaussian and obeys a statistical law established by Einstein in 1905. Along a single direction is space, the average molecular excursion of water molecules is proportional to the square root of diffusion time T_d. Mathematically, this can be expressed as $s = (2DT_d)^{1/2}$, where s is the root-mean-squared distance and D is the diffusion coefficient (Fig 2a). For free water at brain temperatures (37° C), the diffusion coefficient is ~ 3 μm^2/ms (29), which translates to a distance of approximately 17 μm in 50 ms. In brain tissue, however, water molecules are constantly bouncing off and interacting with various tissue elements such as cell membranes and macromolecules. The net result is a decrease in diffusion mobility of water and a displacement distribution that no longer follows a single Gaussian distribution. Generally speaking, tissue elements impede water diffusion both through diffusion hindrance and restriction. Hindered and restricted diffusion are two distinct processes that result from fundamentally different behavior of spins within the intra- and extracellular tissue compartments, as described next.

Hindered diffusion—Hindered diffusion refers to the *delay* of passage of small molecules as they navigate *around* cellular obstacles, as in brain extracellular space (ECS) (Fig 2b). There is a long history (30) of quantifying the degree of hindrance to diffusion in the ECS compared to that of a free medium by the *tortuosity* λ (31), defined simply as the square root of the ratio of the free (or intrinsic) extracellular diffusion coefficient D_{extra} to the measured, or apparent diffusion coefficient for extracellular water ADC_{extra}: $\lambda = (D_{extra}/ADC_{extra})^{1/2}$. As such, tortuosity simply reflects the degree to which the ECS slows diffusion relative to free water. Extensive experimental studies using real-time iontophoresis (RTI) employing the cation tetramethylammonium (TMA) indicate that diffusion through tortuous ECS in normal brain is generally slowed by a factor of about 2.6, corresponding to λ of about 1.6 (31). While there may be several factors that ultimately contribute to the delay of passage of water molecules in brain ECS (such as the composition of the extracellular matrix and the transient trapping or binding of water molecules to cell surfaces, see ref (32)), perhaps the

greatest contribution is ECS geometry (dictated by the extracellular volume fraction α and shape of cells). As α decreases, due to for example cell swelling or greater cell packing density (cellularity), water molecules must travel more circuitous paths *around* cellular obstructions and tortuosity increases. The maximum theoretical tortuosity due to geometry can be quantified as the ratio of the distance though the center of a spherical cell to the distance around the periphery of the cell or $\lambda_g = \pi/2 = 1.57$ (Fig 2, inset). However, more complex simulations over a wide variety of packed cellular objects indicates that the maximum tortuosity due to geometry is no greater than 1.22 (33). In tumor ECS (or "tumor interstitium"), both tortuosity and volume fraction α are generally higher. For example, in anaplastic astrocytomas and glioblastomas, the average α was measured to be as high as 0.47–0.49 with λ around 1.67–1.77 (34). Increased α has been associated with necrosis and or vasogeneic edema, while increased λ may result from either astrogliosis, commonly observed in tumor tissue, or to changes in the extracellular matrix (32, 34). In summary, while it is often suggested that the low ADC observed in high-grade tumors results from increased packing density (cellularity) of cells due to greater hindrance imposed on extracellular water diffusion, from a physical perspective cellular crowding can only mildly reduce the effective diffusion coefficient in tumors (λ increases only narrowly with decreasing α). Therefore, it stands to reason that a major component in decreased ADC in tumors, especially at high b-values, is restricted diffusion *within* the cellular compartments themselves, described next.

Restricted diffusion—Restricted diffusion is a term classically used (35) to describe the trapping of water molecules within an enclosed compartment (i.e., as defined by the cell plasma membrane) such that the net distance traveled is restricted or confined by the compartment dimensions. Although the term "restricted diffusion" is often used in the clinical literature to refer to any reported decrease in ADC, the physics of restricted diffusion is fundamentally different from hindered or free water diffusion. Specifically, for restricted diffusion the net squared displacement of water molecules is sub-linear in time, and therefore non-Gaussian (Fig 2c). In addition, the time evolution of net displacements strongly depends on the size and shape of the restricting compartment as well as the intrinsic intracellular diffusivity D_{intra}. In contradistinction to hindered extracellular water where ADC_{extra} is independent with diffusion time T_d, the effective diffusion coefficient for intracellular water (or ADC_{intra}) decreases with T_d over a finite range as a larger proportion of the spins "bounce off" the plasma membrane.

It is important to note that restricted (or non-Gaussian) diffusion must be discussed within the context of diffusion time, permeability, and the size of the restricting cellular compartments. For instance, in the short-time limit (T_d < 1ms), diffusion is largely unrestricted and dictated by the intrinsic diffusivity of the medium ($ADC_{intra} \sim D_{intra}$), except for a small minority of spins located in close proximity to cell membranes or other barriers. Conversely, in the long-time limit (T_d > 1 s) much greater than the average residence time for water within intra- and extracellular compartments, diffusion is dominated by exchange, and can be accounted for by a single apparent tensor, reflecting the effective medium approximation of the tissue ($ADC_{intra} \sim ADC_{tissue}$). In the intermediate-time regime, relevant to typical clinical DWI acquisitions ($T_d \sim$ 50–100 ms), the diffusion

time is short relative to exchange between intra- and extracellular compartments through the plasma membrane (36), but long enough for water molecules to repeatedly come in contact with and "bounce off" the plasma membrane. In this case the intracellular spins approach a "fill-up" regime, where the displacements of spins are physically restricted by the plasma membrane and therefore dictated by the size and shape of the cellular compartment. Note that in the intermediate-time regime diffusion in the extracellular space remains hindered and behaves according to a classical Gaussian model, where the tortuosity is a function of packing density and extracellular volume fraction (31). Therefore, the total water signal in the intermediate-time regime reflects a superpositioning of hindered and restricted water leading to a nonmonoexponential signal decay at high b-value. As we will see below, separating the restricted water fraction from hindered and free water fraction provides a more sensitive and specific biomarker for tumor cellularity compared with traditional ADC.

Diffusion models

Diffusion models form the fundamental basis through which quantitative information about the underlying tissue microstructure can be gleaned from DWI signals. The typical millimetric scale at which DWI measurements are made (i.e., voxel size) is large compared with the micrometric scale of the underlying physical diffusion process, and therefore the goal of the diffusion model to bridge the gap such that inference can be drawn on a scale much smaller than the voxel dimensions. One of the advantages of DWI over other MRI techniques is that the physical scale probed by the measurements can be adjusted by the experimental variables, namely the diffusion time (T_d) and diffusion-weighting factor (b-value). As we will see, this forms the fundamental basis through which more advanced multi-scale, or non-Gaussian, diffusion models offer insight into compartmental diffusion in cancer and improved imaging biomarkers for tumors. We begin this section with brief introduction of the classic ADC and tensor model for Gaussian diffusion and follow it with a more detailed introduction to Restriction Spectrum Imaging (RSI), a technique developed in our lab for probing tissue microstructure in greater detail.

Apparent diffusion coefficient (ADC)—As a departure from earlier studies in which efforts were made to measure the true diffusion process in biological systems (37), it was suggested in the mid 1980s (24) to model the complex diffusion in tissue using the free (Gaussian) diffusion equation, but replace the intrinsic diffusion coefficient D with a global statistical parameter called the "apparent diffusion coefficient" (ADC). The ADC concept has since been used extensively in the literature as well as clinical oncology as a surrogate marker of tumor cellularity (1–3). In practice, the ADC is estimated by combining the experimental variables (i.e. the magnitude, duration, and temporal spacing of the diffusion gradients) into a single parameter called the diffusion-weighting factor, or b-value (24), and comparing the signal attenuation at one or more non-zero b-values with the baseline signal measured without diffusion weighting (i.e., with a b-value of zero). For Gaussian diffusion, the signal attenuation decays exponentially with the product of the b-value and ADC, and therefore the ADC reflects the slope of the best fit line to the log signal as a function of b-value. The diffusion tensor model (DTI) extends the ADC concept to three-dimensional space, allowing for different ADCs along- and perpendicular to the principal axis of diffusion (38).

The main limitation of the ADC and tensor model as imaging biomarkers for tumors is their strict dependence on a single Gaussian function for the displacement distribution of water molecules within cancer tissue, and therefore a monoexponential dependence on the b-value. While a single Gaussian assumption may be appropriate for data collected over a fairly narrow range of b-values (up to about 1000 s/mm^2), the inferences that can be drawn are limited by lack of specificity. For example, numerous investigators have shown a negative correlation between the tumor ADC values and cellularity (1–3), which is commonly attributed to increased *restricted* diffusion imposed by tumor cells. However, despite increased restricted diffusion, tumor ADC values rarely fall below that of normal appearing white matter (NAWM). This is true even in highly cellular tumors that originate in white matter, such as glioblastoma (GBM) and primary CNS lymphoma (39). One explanation for higher than expected ADC values in these tumors is the presence of vasogenic edema and focal necrosis within the tumor itself, which increase the ADC through reduced *hindrance* imposed on the extracellular water (40, 41). Thus, increased ADC due to edema and necrosis will offset reduced ADC imposed by tumor cells, resulting in lesions that are difficult to discern from NAWM on the basis of the ADC alone. This effect becomes more pronounced as the b-value is reduced due to increasing sensitivity to the fast, hindered water fraction.

Restriction Spectrum Imaging—Over the past decade or so, advances in DWI acquisition and gradient hardware have made it possible to probe a whole new regime of water diffusion in cancer tissue beyond what was previously possible on clinical MRI scanners. Specifically, the application of strong magnetic field gradient pulses has allowed a much greater range of b-values, diffusion directions, and diffusion times to be acquired during a clinical acquisition. As a result, diffusion signals can be made specific to pools of water with very low effective diffusion coefficients, well below the tortuosity limit for ECS water, likely originating from restricted water trapped within the cells themselves (42). Numerous promising methods are emerging to capture and model complex non-Gaussian diffusion in tissue including biexponential (20, 21), stretched exponential (22), and kurtosis models (23), as well as methods to study perfusion-related effects in DWI data at low b-values, such as intravoxel incoherent motion (IVIM) (24). The application and description of many of these techniques for neurooncology applications can be found in an excellent review provided by Maier et al (39). Moreover, techniques are immerging to probe diffusion spectra at ultra short diffusion times on clinical systems using oscillating gradients (43), which hold promise for probing intracelluar structures and alterations in cancer (44). For this review, we focus on one particular technique developed in our lab call Restriction Spectrum Imaging (RSI). Over the last few years, RSI has gained increased recognition as an important tool in oncology that overcomes many of the limitation of traditional DWI and ADC.

Restriction spectrum imaging (RSI) is a general framework for modeling diffusion signals collected across a broad range of experimental parameters and relating these signals to underlying tissue parameters (e.g. size and shape/orientation of hindered and restricted water compartments) using a linear mixture model (45). The ultimate goal of RSI is enable quantitative estimates of tissue microstructure based on noninvasive imaging. In order to achieve this, the diffusion signal is modeled as reflecting a mixture of components, where

each component describes the signal dependence on specific tissue properties (e.g. cell size, density, orientation, etc.) as a function of the experimental (protocol) settings (e.g. b-value, diffusion time, echo time, etc). The total signal becomes the weighted sum of these components, and the goal is to determine the individual weights. This is achieved through the application of generalized linear estimation techniques (45, 46). As such, the RSI framework is designed to strike a balance between model complexity and interpretability by minimizing a priori assumptions on microstructure, while preserving biophysical interpretability of the resulting estimates.

Our current clinical implementation RSI acquires data with b-values of 500, 1500, and 4000 s/mm^2 and multiple diffusion directions at each b-value at a fixed intermediate diffusion time (~90 ms), where intracellular spins would be expected to be in the fill-up regime. The RSI design matrix includes a distribution (or “spectrum”) of effective diffusion pools spanning hindered and restricted length scales with both isotropic and anisotropic geometries. In Fig 4 we illustrate both a schematic for the RSI spectrum model and the resultant fit of the model to data collected in a 51 year-old patient with right frontal GBM prior to surgical intervention (47). Note the separation of diffusion components in different tissue types, with the primary lesion exhibiting a large volume fraction of spherically-restricted water likely stemming from water trapped within cancer cells. Also note the large fraction of free and hindered water in areas of necrosis and edema. The volume fraction of spherically restricted water (either with or without additional filtering of white matter signal using a technique called “beamforming” (48)) has been coined the RSI cellularity index or cellularity map (47, 49–51). In addition, the signal from the restricted anisotropic component can be use to map the density and orientation of surrounding white matter tracts (50).

In summary, advanced DWI methods such as RSI that acquire data over an extended b-value range provide the ability to quantify complex non-Gaussian diffusion in tissue (21–23, 52, 53). While these emerging techniques offer a new class of cancer imaging biomarkers, there remains many unanswered questions and tremendous opportunity for further advancing the field. Of particular importance is to understand exactly how parameters of the diffusion model relate to specific properties of cancer tissue, such as tumor cell size, density, and nuclear volume fraction. How specific are these biomarkers to tumor cells versus healthy or inflammatory cells? Can these new imaging biomarkers characterize tumor cytotypes and address a top challenge posed by the NCI to develop *in vivo* imaging methods that can *probe the identity, quantity, and location of different cells that make up a tumor and its microenvironment ?* [NIH RFA-CA-13-020]. Finally, to what extent can these new imaging biomarkers help solve current clinical dilemmas in oncology such as distinguishing tumor recurrence from radiation injury? Answering these questions will undoubtedly require both advances in diffusion modeling, simulation, and MRI hardware and software (such as the latest ultra high performance (“connectome”) MRI scanners (54)) together with improved quantitative histology, multimodal image registration, and validation procedures.

CLINICAL APPLICATIONS OF RSI

Due to its ability to isolate areas of truly *restricted* diffusion by separating and removing the hindered diffusion signal, RSI offers a more direct measure of tumor cells than other

diffusion weighted methods. Within the past year, we have shown that by identifying areas of restricted diffusion, RSI can be applied clinically to *1)* improve tumor conspicuity in patients with high-grade primary and metastatic brain tumors (47), *2)* facilitate the interpretation of tumor response on imaging following anti-angiogenic treatments that significantly reduce edema (49), and *3)* improve the ability to visualize white matter pathways coursing through regions of peritumoral edema relative to standard DTI (50). In the following sections, we describe each of these clinical applications in further detail. In addition, we describe a clinical scenario in which RSI lacks specificity and a multispectral imaging approach is warranted.

Improved conspicuity of High Grade Tumors with RSI

As described in the introduction, ADC is frequently used as a marker of tumor cellularity in patients with high-grade tumors (1–3). Areas of tumor are associated with decreased ADC relative to surrounding tissue (40). However, concomitant edema and tumor-related necrosis increase ADC values, thereby directly opposing the reduction in ADC associated with tumor (55, 56). This offset presents a diagnostic challenge by diminishing the conspicuity of tumor on ADC maps. Because RSI isolates areas of spherically-restricted diffusion, we tested whether it could provide increased conspicuity and delineation of tumor margins relative to standard and high b-value ADC (57). To accomplish this, RSI was performed in 10 pre-surgical patients: 4 with glioblastoma, 3 with primary CNS lymphoma, and 3 with metastatic brain tumors. Tumor conspicuity, edema conspicuity, and relative sensitivity to edema were quantified for RSI-cellularity maps (CMs), high b-value DWI (b = 4000), and ADC, and these values were compared in manually drawn volumes of interest. Receiver operating characteristic (ROC) curves were used to evaluate the sensitivity and specificity of each method for delineating tumor from normal appearing white matter (NAWM). In addition to visible differences in conspicuity (Fig 5), ROC curves revealed greater sensitivity and specificity for delineating tumor from NAWM with RSI-CM (AUC=.91) compared with both high b-value DWI (AUC=.77) and ADC (AUC=.66). In addition, the relative sensitivity to edema was greater for high b-value DWI and ADC compared to RSI, reflecting RSI's ability to suppress the fast diffusion component associated with edema. Furthermore, greater heterogeneity of the diffusion signal within tumor was observed on the RSI-CMs compared to DWI and ADC, as evidenced by a broader histogram distribution. This may represent the intrinsic heterogeneity of tumor cellularity both within and across tumor types. These data demonstrate one promising application of RSI, i.e., improved conspicuity and delineation of high-grade tumors compared to traditional DWI models, and underscore the possibility that RSI may prove helpful in delineating tumor cytotypes and infiltrating disease in peritumoral edema

RSI in the context of antiangiogenic treatment

Antiangiogenic therapies, such as bevacizumab, are increasingly used in the treatment of recurrent high-grade gliomas. However, these agents decrease permeability of the blood-brain barrier, and therefore, decrease contrast enhancement and edema in patients with high-grade gliomas in a manner that may not correlate with actual tumor response—a phenomenon known as *pseudoresponse* (58). Given this imaging challenge, we evaluated the ability of RSI to improve conspicuity within regions of tumor compared to ADC in

patients treated with bevacizumab, and to further demonstrate that RSI is minimally affected by bevacizumab-induced reductions in edema (49). RSI-CMs and DWI were available for a series of patients with recurrent gliomas at baseline and following initiation of bevacizumab. Results showed that all patients exhibited sharp decreases in contrast enhancement and edema following treatment (i.e., *pseudoresponse*). Bevacizumab-induced decreases in edema had a greater effect on ADC than on the RSI-CMs, with the relative sensitivity to changes in edema being over 20 times higher on ADC than on RSI-CMs (Fig. 6). These data provide additional evidence that RSI is less influenced by changes in edema compared to ADC, which may confer an advantage of RSI for interpreting *true* tumor response in the setting of antiangiogenic treatment. However, this study did not include clinical follow-up. Thus, whether RSI has greater predictive validity than ADC is of key importance and requires additional investigation.

RSI for improved delineation of white matter tracts

There is increasing enthusiasm for the use of DTI and tractography in neurosurgical planning (59–66), and there is some evidence that tractography-guided neuronavigation can be used to minimize neurological morbidity (62, 67, 68). However, the ability to resolve white matter structure in peritumoral regions that include edema has remained a challenge (69, 70). We applied the same logic as in the previous examples and tested the ability of RSI to provide better visualization and quantification of white matter tracts in regions that include edema(50). In this example, isolating the slow, restricted compartment yields a better estimate of “tubularity” (i.e., models the cylindrically-restricted diffusion within axons)(45). This increases the sharpness of the estimates, allowing for better delineation of fiber tract orientation. In a series of 10 patients with high-grade gliomas, we were able to demonstrate that RSI yielded higher fractional anisotropy (FA) estimates in regions of edema relative to standard DTI. Furthermore, at follow-up when the edema had resolved in most patients, FA estimates increased with DTI, but remained stable with RSI, indicating that FA estimates based on DTI were artificially suppressed by the edema. Tractography performed within regions of edema revealed superior ability of RSI to track fibers through areas of significant edema relative to standard DTI (Fig 7). These data address yet another important and growing application of diffusion imaging within the field of neuro-oncology (i.e., surgical planning) and speak to the advantage of using advanced DWI models for revealing the anatomical structure of peritumoral white matter. An important caveat to mention is that it is well known that gliomas grow via an infiltrative pattern and that there is often non-enhancing infiltrating tumor surrounding the enhancing portion of a high-grade glioma (71). Further investigation is required to determine whether RSI or other advanced DWI methods will prove useful for detecting these areas of tumor infiltration.

Importance of a Multispectral Imaging Approach

Despite the many recent advancements in MR technology and DWI methods, no single modality has emerged as the “holy grail” of tumor imaging. Thus, most diagnostic challenges in neuro-oncology are best addressed using a multispectral imaging approach. One particular challenge occurs following treatment with concurrent bevacizumab and radiation therapy, with a subset of patients developing regions of marked and persistent restricted diffusion that do not appear to reflect aggressive tumor (72–74). Although the

etiology of these lesions remains uncertain, pathologic confirmation in several patients has revealed atypical gelatinous necrosis. We have coined this abnormality *bevacizumab-related imaging abnormality (BRIA)* and have observed that the BRIA signal on RSI is quantitatively similar to that seen in tumor (51). This illustrates a clinical scenario in which RSI lacks specificity and a multispectral imaging approach is warranted. Thus, we explored whether using RSI in combination with perfusion imaging could help to differentiate BRIA from recurrent tumor. In a series of patients, we show that these techniques are complementary in that RSI is superior to rCBV for differentiating pathology from NAWM, whereas rCBV is superior for differentiating BRIA from tumor (Fig 8). Thus, the combination of high RSI signal and low rCBV provides a distinct imaging signature of the BRIA phenomenon. Because of the increasing use of anti-angiogenic agents, imaging methods that increase our understanding of both pseudoresponse and BRIA are of high importance. These data highlight an important example in which RSI lacks specificity in its current instantiation and information from complementary imaging modalities is essential.

RSI for improved detection of other solid organ tumors

Although this review is primarily focused on neuro-oncology applications, quantitative imaging is equally relevant to other solid organ tumors. For example, multiparametric MRI has been explored in a variety of applications, including discrimination between indolent and aggressive disease in prostate cancer. Routine T_2-weighted imaging of the prostate is the most sensitive way to evaluate anatomical detail, but is limited for disease detection with sensitivity of around 70% and specificity of 55% (75). Functional MR techniques enhance detection, grading and staging of prostate cancer through the use of dynamic contrast enhancement (DCE), diffusion weighted imaging (DWI) and MR spectroscopic imaging. DCE requires IV administration of a T1-shortening agent with the chief limitation being that the maximum contrast enhancement between malignant and non-aggressive disease is small (76). MR spectroscopic imaging increases specificity (77, 78), but is technically challenging and can add significantly to scan time.

Multiple studies have shown that DWI improves sensitivity and specificity in the diagnosis of prostate cancer by increasing tumor conspicuity on DWI or quantitative apparent diffusion coefficient (ADC) maps. However, hemorrhage, inflammatory processes and benign nodules in the transitional zone can all exhibit lower ADC values leading to false positives (79). DWI can also suffer from severe spatial distortion limiting its co-registration to anatomic images, which is necessary for tumor localization.

Increasing Gleason score correlates with loss of normal gland formation, loss of peripheral gland tubular structure and increased cellularity (80). We hypothesize, therefore, that RSI Cellularity will correlate with higher tumor grade, as measured by Gleason score, and will provide significantly greater accuracy in discriminating aggressive tumor from benign and indolent lesions when compared to current functional or anatomical imaging techniques.

Our preliminary data are encouraging. Figure 9 shows a patient with Gleason 3+4 = 7 disease. RSI cellularity map is shown color-coded and fused with the T2, after spatial distortion correction and registration. Note the correspondence of RSI celluarity with the histopathology slice. T2 and perfusion images are not as conspicuous, with much less

contrast to noise ratio. This represents an example case in which conventional imaging is not as diagnostic.

Importance of Spatial Distortion Correction for Accurate Image-guided Intervention

One of the main limitations of diffusion imaging in general is nonlinear spatial distortion of the images due to a number of factors, including gradient nonlinearities, eddy currents, and B_0 field inhomogeneities. While distortions due to nonlinearities of the gradient fields are commonly corrected for by software on the scanner console, B_0 field inhomogeneities are not, despite being the dominant source of spatial inaccuracy in DWI. The magnitude of B_0 distortions varies depending on a number of factors, including field strength, positioning of the subject within the scanner, and subject specific anatomy. The typical pattern of B_0 distortion on 3T systems is illustrated in Fig 8, along with the total whole brain histogram of root mean square (RMS) displacements. As illustrated in the figure, on average (based scans from on 40 subjects) the typical (mode) distortion magnitude is approximately 4 mm, with a substantial proportion of voxels displaced more than 10 mm. Such distortions are of particular concern when images are used for image-guided intervention, including surgery, biopsy, or radiation dose planning. Although methods for correcting B_0 distortions have existed for some time (81–83), they are typically used only in research studies, and not in clinical practice, primarily due to the additional scan time required to acquire the B_0 field maps required for standard correction methods. The method introduced by Holland et al (84) overcomes this limitation by requiring only a single additional TR (2–3 seconds), using the reverse phase-encode polarity method (82, 85, 86). Moreover, this additional volume acquisition can be integrated directly in the native DWI protocol without changing the pulse-sequence. Combined with efficient post processing methods to estimate the distortion field (84), the reverse phase encode polarity technique provides a much needed clinical solution for accurate spatial distortion correction of DWI data. The RSI technique incorporates this procedure as part of standard preprocessing of data, and all the data presented in this review has been corrected in this manner.

DISCUSSION AND CONCLUSION

The field of MR imaging is rapidly evolving, leading to new and exciting possibilities within neuro-oncology, urological oncology and beyond. In particular, the development of advanced DWI methods has allowed for improved visualization and detection of tumor cells and thus has great potential for better understanding of tumor biology. Numerous clinical applications of this powerful technique have already been demonstrated, including tumor characterization and grading, prognostication, early prediction of response to therapy and survival, distinguishing tumor from treatment-related confounds, detecting microinfiltration, and guiding neurosurgical and radiation planning (87). However, future advances in the field will require a fundamental understanding of the underlying DWI signal coupled with validation of diffusion contrast in unique tumor-related pathologies. In addition to improved detection of tumors, advanced diffusion methods such as RSI may also provide quantitative characterization of cellular properties such as cell size, permeability, and nuclear volume fraction, based on signal variation as a function of diffusion time and echo time (42). Validation of these measures will likely be borne out of translational efforts that include

both preclinical and clinical studies in which histological specimens are carefully co-registered to in vivo imaging. The need for targeted biopsies based on advanced DWI, precise co-registration of DWI with other imaging modalities, and careful corrections for geometric distortions will all be pivotal to providing the spatial precision needed to achieve such validation. These requirements underscore the need for a multidisciplinary approach to this validation including experts in the fields of Oncology, Surgery, Pathology, and Radiology. Through this collaboration, not only will current applications of DWI be further improved, but new possibilities will also be created that will ultimately lead to better care for patients suffering from cancer.

Acknowledgments

Funding: grants R01AG031224, R01EB000790, RC2 DA29475 (A.M.D.)

We would like to thank patients at UC San Diego Neuro-Oncology Program for their generous participation

References

1. Sugahara T, Korogi Y, Kochi M, Ikushima I, Shigematu Y, Hirai T, et al. Usefulness of diffusion-weighted MRI with echo-planar technique in the evaluation of cellularity in gliomas. J Magn Reson Imaging. 1999; 9:53–60. [PubMed: 10030650]
2. Chen J, Xia J, Zhou YC, Xia LM, Zhu WZ, Zou ML, et al. Correlation between magnetic resonance diffusion weighted imaging and cell density in astrocytoma. Zhonghua Zhong Liu Za Zhi. 2005; 27:309–11. [PubMed: 15996330]
3. Guo AC, Cummings TJ, Dash RC, Provenzale JM. Lymphomas and high-grade astrocytomas: comparison of water diffusibility and histologic characteristics. Radiology. 2002; 224:177–83. [PubMed: 12091680]
4. Hilario A, Ramos A, Perez-Nunez A, Salvador E, Millan JM, Lagares A, et al. The added value of apparent diffusion coefficient to cerebral blood volume in the preoperative grading of diffuse gliomas. AJNR American journal of neuroradiology. 2012; 33:701–7. [PubMed: 22207304]
5. Server A, Kulle B, Maehlen J, Josefsen R, Schellhorn T, Kumar T, et al. Quantitative apparent diffusion coefficients in the characterization of brain tumors and associated peritumoral edema. Acta Radiol. 2009; 50:682–9. [PubMed: 19449234]
6. Toh CH, Castillo M, Wong AM, Wei KC, Wong HF, Ng SH, et al. Primary cerebral lymphoma and glioblastoma multiforme: differences in diffusion characteristics evaluated with diffusion tensor imaging. AJNR Am J Neuroradiol. 2008; 29:471–5. [PubMed: 18065516]
7. Wang W, Steward CE, Desmond PM. Diffusion tensor imaging in glioblastoma multiforme and brain metastases: the role of p, q, L, and fractional anisotropy. AJNR American journal of neuroradiology. 2009; 30:203–8. [PubMed: 18842762]
8. Wang S, Kim S, Chawla S, Wolf RL, Zhang WG, O'Rourke DM, et al. Differentiation between glioblastomas and solitary brain metastases using diffusion tensor imaging. Neuroimage. 2009; 44:653–60. [PubMed: 18951985]
9. Yamasaki F, Kurisu K, Satoh K, Arita K, Sugiyama K, Ohtaki M, et al. Apparent diffusion coefficient of human brain tumors at MR imaging. Radiology. 2005; 235:985–91. [PubMed: 15833979]
10. Tomura N, Narita K, Izumi J, Suzuki A, Anbai A, Otani T, et al. Diffusion changes in a tumor and peritumoral tissue after stereotactic irradiation for brain tumors: possible prediction of treatment response. J Comput Assist Tomogr. 2006; 30:496–500. [PubMed: 16778628]
11. Schmainda KM. Diffusion-weighted MRI as a biomarker for treatment response in glioma. CNS oncology. 2012; 1:169–80. [PubMed: 23936625]
12. Babsky AM, Hekmatyar SK, Zhang H, Solomon JL, Bansal N. Predicting and monitoring response to chemotherapy by 1,3-bis(2-chloroethyl)-1-nitrosourea in subcutaneously implanted 9L glioma

using the apparent diffusion coefficient of water and 23Na MRI. J Magn Reson Imaging. 2006; 24:132–9. [PubMed: 16758478]

13. Oh J, Henry RG, Pirzkall A, Lu Y, Li X, Catalaa I, et al. Survival analysis in patients with glioblastoma multiforme: predictive value of choline-to-N-acetylaspartate index, apparent diffusion coefficient, and relative cerebral blood volume. J Magn Reson Imaging. 2004; 19:546–54. [PubMed: 15112303]
14. Pope WB, Lai A, Mehta R, Kim HJ, Qiao J, Young JR, et al. Apparent diffusion coefficient histogram analysis stratifies progression-free survival in newly diagnosed bevacizumab-treated glioblastoma. AJNR Am J Neuroradiol. 32:882–9. [PubMed: 21330401]
15. Nakamura H, Murakami R, Hirai T, Kitajima M, Yamashita Y. Can MRI-derived factors predict the survival in glioblastoma patients treated with postoperative chemoradiation therapy? Acta Radiol. 2013; 54:214–20. [PubMed: 23138021]
16. Pope WB, Mirsadraei L, Lai A, Eskin A, Qiao J, Kim HJ, et al. Differential gene expression in glioblastoma defined by ADC histogram analysis: relationship to extracellular matrix molecules and survival. AJNR American journal of neuroradiology. 2012; 33:1059–64. [PubMed: 22268080]
17. Saksena S, Jain R, Narang J, Scarpace L, Schultz LR, Lehman NL, et al. Predicting survival in glioblastomas using diffusion tensor imaging metrics. Journal of magnetic resonance imaging : JMRI. 2010; 32:788–95. [PubMed: 20882608]
18. Wedeen VJ, Hagmann P, Tseng WY, Reese TG, Weisskoff RM. Mapping complex tissue architecture with diffusion spectrum magnetic resonance imaging. Magn Reson Med. 2005; 54:1377–86. [PubMed: 16247738]
19. Tuch DS. Q-ball imaging. Magn Reson Med. 2004; 52:1358–72. [PubMed: 15562495]
20. Maier SE, Bogner P, Bajzik G, Mamata H, Mamata Y, Repa I, et al. Normal brain and brain tumor: multicomponent apparent diffusion coefficient line scan imaging. Radiology. 2001; 219:842–9. [PubMed: 11376280]
21. Mulkern RV, Gudbjartsson H, Westin CF, Zengingonul HP, Gartner W, Guttmann CR, et al. Multi-component apparent diffusion coefficients in human brain. NMR Biomed. 1999; 12:51–62. [PubMed: 10195330]
22. Bennett KM, Schmainda KM, Bennett RT, Rowe DB, Lu H, Hyde JS. Characterization of continuously distributed cortical water diffusion rates with a stretched-exponential model. Magn Reson Med. 2003; 50:727–34. [PubMed: 14523958]
23. Jensen JH, Helpern JA, Ramani A, Lu H, Kaczynski K. Diffusional kurtosis imaging: the quantification of non-gaussian water diffusion by means of magnetic resonance imaging. Magn Reson Med. 2005; 53:1432–40. [PubMed: 15906300]
24. Le Bihan D, Breton E, Lallemand D, Grenier P, Cabanis E, Laval-Jeantet M. MR imaging of intravoxel incoherent motions: application to diffusion and perfusion in neurologic disorders. Radiology. 1986; 161:401–7. [PubMed: 3763909]
25. Merboldt K-D, Hanicke W, Frahm J. Self-diffusion NMR imaging using stimulated echoes. Journal of Magnetic Resonance (1969). 1985; 64:479–86.
26. Le Bihan D, Breton E. Imagerie de diffusion in-vivo par résonance. C R Acad Sci (Paris). 1985; 301:1109–12.
27. Taylor DG, Bushell MC. The spatial mapping of translational diffusion coefficients by the NMR imaging technique. Phys Med Biol. 1985; 30:345–9. [PubMed: 4001161]
28. Stejskal EO, Tanner JE. Spin diffusion measurements: Spin echoes in the presence of a time-dependent field gradient. J Chem Phys. 1965; 42:288–92.
29. Le Bihan D. Looking into the functional architecture of the brain with diffusion MRI. Nat Rev Neurosci. 2003; 4:469–80. [PubMed: 12778119]
30. Harris EJ, Burn GP. The transfer of sodium and potassium ions between muscle and the surrounding medium. Transactions of the Faraday Society. 1949; 45:508–28.
31. Nicholson C. Diffusion and related transport mechanisms in brain tissue. Reports on Progress in Physics. 2001; 64:815.
32. Sykova E, Nicholson C. Diffusion in brain extracellular space. Physiol Rev. 2008; 88:1277–340. [PubMed: 18923183]

33. Tao L, Nicholson C. Maximum geometrical hindrance to diffusion in brain extracellular space surrounding uniformly spaced convex cells. J Theor Biol. 2004; 229:59–68. [PubMed: 15178185]
34. Vargova L, Homola A, Zamecnik J, Tichy M, Benes V, Sykova E. Diffusion parameters of the extracellular space in human gliomas. Glia. 2003; 42:77–88. [PubMed: 12594739]
35. Le Bihan D. Molecular diffusion, tissue microdynamics and microstructure. NMR Biomed. 1995; 8:375–86. [PubMed: 8739274]
36. Stanisz GJ. Diffusion MR in Biological Systems: Tissue Compartments and Exchange. Israel Journal of Chemistry. 2003; 43:33–44.
37. Tanner JE. Transient diffusion in a system partitioned by permeable barriers. Application to NMR measurements with a pulsed field gradient. The Journal of Chemical Physics. 1978; 69:1748–54.
38. Basser PJ, Mattiello J, LeBihan D. MR diffusion tensor spectroscopy and imaging. Biophys J. 1994; 66:259–67. [PubMed: 8130344]
39. Maier SE, Sun Y, Mulkern RV. Diffusion imaging of brain tumors. NMR Biomed. 2010; 23:849–64. [PubMed: 20886568]
40. Chenevert TL, Sundgren PC, Ross BD. Diffusion imaging: insight to cell status and cytoarchitecture. Neuroimaging Clin N Am. 2006; 16:619–32. viii–ix. [PubMed: 17148023]
41. Nicholson C. Factors governing diffusing molecular signals in brain extracellular space. J Neural Transm. 2005; 112:29–44. [PubMed: 15372328]
42. White N, Dale A. Distinct effects of nuclear volume fraction and cell diameter on high b-value diffusion MRI contrast in tumors. Mag Res Med. 2013 In Press.
43. Gore JC, Xu J, Colvin DC, Yankeelov TE, Parsons EC, Does MD. Characterization of tissue structure at varying length scales using temporal diffusion spectroscopy. NMR Biomed. 2010; 23:745–56. [PubMed: 20677208]
44. Xu J, Li K, Smith RA, Waterton JC, Zhao P, Chen H, et al. Characterizing tumor response to chemotherapy at various length scales using temporal diffusion spectroscopy. PLoS One. 2012; 7:e41714. [PubMed: 22911846]
45. White NS, Leergaard TB, D'Arceuil H, Bjaalie JG, Dale AM. Probing tissue microstructure with restriction spectrum imaging: Histological and theoretical validation. Hum Brain Mapp. 2013; 34:327–46. [PubMed: 23169482]
46. White NS, Dale AM. Optimal diffusion MRI acquisition for fiber orientation density estimation: an analytic approach. Hum Brain Mapp. 2009; 30:3696–703. [PubMed: 19603409]
47. White NS, McDonald CR, Farid N, Kuperman JM, Kesari S, Dale AM. Improved conspicuity and delineation of high-grade primary and metastatic brain tumors using "restriction spectrum imaging": quantitative comparison with high B-value DWI and ADC. AJNR Am J Neuroradiol. 2013; 34:958–64. S1. [PubMed: 23139079]
48. White, NS.; Kuperman, J.; McDonald, CR.; Farid, N.; Kasai, K.; Shankaranarayanan, A., et al. Restriction Spectrum Imaging of Glioblastoma Multiform: Comparison with ADC. 20th Annual Meeting ISMRM; 2012; Melbourne, Australia.
49. Kothari PD, White NS, Farid N, Chung R, Kuperman JM, Girard HM, et al. Longitudinal restriction spectrum imaging is resistant to pseudoresponse in patients with high-grade gliomas treated with bevacizumab. AJNR Am J Neuroradiol. 2013; 34:1752–7. [PubMed: 23578667]
50. McDonald CR, White NS, Farid N, Lai G, Kuperman JM, Bartsch H, et al. Recovery of white matter tracts in regions of peritumoral FLAIR hyperintensity with use of restriction spectrum imaging. AJNR Am J Neuroradiol. 2013; 34:1157–63. [PubMed: 23275591]
51. Farid N, Almeida-Freitas DB, White NS, McDonald CR, Muller KA, Vandenberg SR, et al. Restriction-Spectrum Imaging of Bevacizumab-Related Necrosis in a Patient with GBM. Front Oncol. 2013; 3:258. [PubMed: 24137566]
52. White N, Leergaard T, D'Arceuil H, Bjaalie J, Dale A. Probing tissue microstructure with restriction spectrum imaging: histological and theoretical validation. Human Brain Mapping. In Press.
53. Parsons EC, Does MD, Gore JC. Temporal diffusion spectroscopy: Theory and implementation in restricted systems using oscillating gradients. Magnetic Resonance in Medicine. 2006; 55:75–84. [PubMed: 16342147]

54. McNab JA, Edlow BL, Witzel T, Huang SY, Bhat H, Heberlein K, et al. The Human Connectome Project and beyond: initial applications of 300 mT/m gradients. Neuroimage. 2013; 80:234–45. [PubMed: 23711537]
55. Castillo M, Smith JK, Kwock L, Wilber K. Apparent diffusion coefficients in the evaluation of high-grade cerebral gliomas. American Journal of Neuroradiology. 2001; 22:60–4. [PubMed: 11158889]
56. Stadnik TW, Chaskis C, Michotte A, Shabana WM, van Rompaey K, Luypaert R, et al. Diffusion-weighted MR imaging of intracerebral masses: comparison with conventional MR imaging and histologic findings. American Journal of Neuroradiology. 2001; 22:969–76. [PubMed: 11337344]
57. White NS, McDonald CR, Farid N, Kuperman JM, Kesari S, Dale AM. Improved Conspicuity and Delineation of High-Grade Primary and Metastatic Brain Tumors Using “Restriction Spectrum Imaging”: Quantitative Comparison with High B-Value DWI and ADC. AJNR Am J Neuroradiol. in press.
58. Jain RK. Normalization of tumor vasculature: an emerging concept in antiangiogenic therapy. Science. 2005; 307:58–62. [PubMed: 15637262]
59. Kamada K, Todo T, Masutani Y, Aoki S, Ino K, Takano T, et al. Combined use of tractography-integrated functional neuronavigation and direct fiber stimulation. J Neurosurg. 2005; 102:664–72. [PubMed: 15871509]
60. Nimsky C, Ganslandt O, Hastreiter P, Wang R, Benner T, Sorensen AG, et al. Preoperative and intraoperative diffusion tensor imaging-based fiber tracking in glioma surgery. Neurosurgery. 2005; 56:130–7. discussion 8. [PubMed: 15617595]
61. Mori S, Frederiksen K, van Zijl PC, Stieltjes B, Kraut MA, Solaiyappan M, et al. Brain white matter anatomy of tumor patients evaluated with diffusion tensor imaging. Ann Neurol. 2002; 51:377–80. [PubMed: 11891834]
62. Yu CS, Li KC, Xuan Y, Ji XM, Qin W. Diffusion tensor tractography in patients with cerebral tumors: a helpful technique for neurosurgical planning and postoperative assessment. Eur J Radiol. 2005; 56:197–204. [PubMed: 15916876]
63. Kamada K, Houkin K, Takeuchi F, Ishii N, Ikeda J, Sawamura Y, et al. Visualization of the eloquent motor system by integration of MEG, functional, and anisotropic diffusion-weighted MRI in functional neuronavigation. Surg Neurol. 2003; 59:352–61. discussion 61–2. [PubMed: 12765803]
64. Duffau H, Thiebaut de Schotten M, Mandonnet E. White matter functional connectivity as an additional landmark for dominant temporal lobectomy. J Neurol Neurosurg Psychiatry. 2008; 79:492–5. [PubMed: 18408087]
65. Nimsky C, Ganslandt O, von Keller B, Fahlbusch R. Preliminary experience in glioma surgery with intraoperative high-field MRI. Acta Neurochir Suppl. 2003; 88:21–9. [PubMed: 14531557]
66. Nimsky C, Grummich P, Sorensen AG, Fahlbusch R, Ganslandt O. Visualization of the pyramidal tract in glioma surgery by integrating diffusion tensor imaging in functional neuronavigation. Zentralbl Neurochir. 2005; 66:133–41. [PubMed: 16116556]
67. Sun GC, Chen XL, Zhao Y, Wang F, Hou BK, Wang YB, et al. Intraoperative high-field magnetic resonance imaging combined with fiber tract neuronavigation-guided resection of cerebral lesions involving optic radiation. Neurosurgery. 2011; 69:1070–84. [PubMed: 21654536]
68. Bello L, Gambini A, Castellano A, Carrabba G, Acerbi F, Fava E, et al. Motor and language DTI Fiber Tracking combined with intraoperative subcortical mapping for surgical removal of gliomas. Neuroimage. 2008; 39:369–82. [PubMed: 17911032]
69. Kinoshita M, Yamada K, Hashimoto N, Kato A, Izumoto S, Baba T, et al. Fiber-tracking does not accurately estimate size of fiber bundle in pathological condition: initial neurosurgical experience using neuronavigation and subcortical white matter stimulation. Neuroimage. 2005; 25:424–9. [PubMed: 15784421]
70. Maier SE, Sun Y, Mulkern RV. Diffusion imaging of brain tumors. NMR Biomed. 23:849–64. [PubMed: 20886568]
71. Kesari S. Understanding glioblastoma tumor biology: the potential to improve current diagnosis and treatments. Seminars in oncology. 2011; 38 (Suppl 4):S2–10. [PubMed: 22078644]

72. Mong S, Ellingson BM, Nghiemphu PL, Kim HJ, Mirsadraei L, Lai A, et al. Persistent diffusion-restricted lesions in bevacizumab-treated malignant gliomas are associated with improved survival compared with matched controls. AJNR American journal of neuroradiology. 2012; 33:1763–70. [PubMed: 22538078]
73. Jeyaretna DS, Curry WT Jr, Batchelor TT, Stemmer-Rachamimov A, Plotkin SR. Exacerbation of cerebral radiation necrosis by bevacizumab. Journal of clinical oncology : official journal of the American Society of Clinical Oncology. 2011; 29:e159–62. [PubMed: 21149667]
74. Rieger J, Bahr O, Muller K, Franz K, Steinbach J, Hattingen E. Bevacizumab-induced diffusion-restricted lesions in malignant glioma patients. Journal of neuro-oncology. 2010; 99:49–56. [PubMed: 20035366]
75. Kirkham AP, Emberton M, Allen C. How good is MRI at detecting and characterising cancer within the prostate? Eur Urol. 2006; 50:1163–74. discussion 75. [PubMed: 16842903]
76. Bonekamp D, Macura KJ. Dynamic contrast-enhanced magnetic resonance imaging in the evaluation of the prostate. Top Magn Reson Imaging. 2008; 19:273–84. [PubMed: 19512849]
77. Kurhanewicz J, Vigneron DB, Hricak H, Narayan P, Carroll P, Nelson SJ. Three-dimensional H-1 MR spectroscopic imaging of the in situ human prostate with high (0.24–0.7-cm3) spatial resolution. Radiology. 1996; 198:795–805. [PubMed: 8628874]
78. Weinreb JC, Blume JD, Coakley FV, Wheeler TM, Cormack JB, Sotto CK, et al. Prostate cancer: sextant localization at MR imaging and MR spectroscopic imaging before prostatectomy--results of ACRIN prospective multi-institutional clinicopathologic study. Radiology. 2009; 251:122–33. [PubMed: 19332850]
79. Yoshimitsu K, Kiyoshima K, Irie H, Tajima T, Asayama Y, Hirakawa M, et al. Usefulness of apparent diffusion coefficient map in diagnosing prostate carcinoma: correlation with stepwise histopathology. J Magn Reson Imaging. 2008; 27:132–9. [PubMed: 18050334]
80. Langer DL, van der Kwast TH, Evans AJ, Plotkin A, Trachtenberg J, Wilson BC, et al. Prostate tissue composition and MR measurements: investigating the relationships between ADC, T2, K(trans), v(e), and corresponding histologic features. Radiology. 2010; 255:485–94. [PubMed: 20413761]
81. Jezzard P, Balaban RS. Correction for geometric distortion in echo planar images from B(o) field variations. Magnetic resonance in medicine. 1995; 34:65–73. [PubMed: 7674900]
82. Andersson JLR, Skare S, Ashburner J. How to correct susceptibility distortions in spin-echo echo-planar images: Application to diffusion tensor imaging. Neuroimage. 2003; 20:870–88. [PubMed: 14568458]
83. Robson MD, Gore JC, Constable RT. Measurement of the point spread function in MRI using constant time imaging. Magnetic resonance in medicine. 1997; 38:733–40. [PubMed: 9358447]
84. Holland D, Kuperman JM, Dale AM. Efficient correction of inhomogeneous static magnetic field-induced distortion in Echo Planar Imaging. Neuroimage. 2010; 50:175–83. [PubMed: 19944768]
85. Morgan PS, Bowtell RW, McIntyre DJO, Worthington BS. Correction of Spatial Distortion in EPI Due to Inhomogeneous Static Magnetic Fields Using the Reversed Gradient Method. Journal of magnetic resonance imaging. 2004; 19:499–507. [PubMed: 15065175]
86. Chang H, Fitzpatrick JM. A technique for accurate magnetic resonance imaging in the presence of field inhomogeneities. IEEE Transactions on Medical Imaging. 1992; 11:319–29. [PubMed: 18222873]
87. Gerstner ER, Sorensen AG. Diffusion and diffusion tensor imaging in brain cancer. Semin Radiat Oncol. 2011; 21:141–6. [PubMed: 21356481]

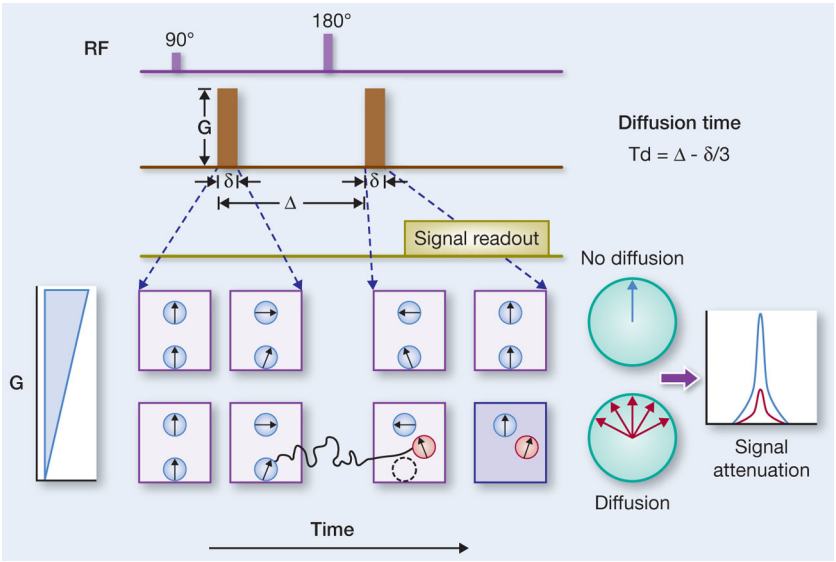

Figure 1.

The diffusion experiment. Sensitivity to the random molecular displacements (Brownian motion) of water molecules is achieved through the use to two magnetic field gradient pulses with amplitude G, duration δ, and separation Δ. During the first pulse, the initial positions of water molecules (spins) are encoded with a phase offset depending on their spatial location in the gradient field. The second pulse is then applied after some finite delay Δ to realign the spin phases. In this way, if water molecules diffusion to a different physical location *along* the gradient field direction, refocusing will be imperfect and a net phase dispersion will result. This phase dispersion causes an attenuation of the magnitude signal and a decrease (darkening) of the measurement voxel in the reconstructed image.

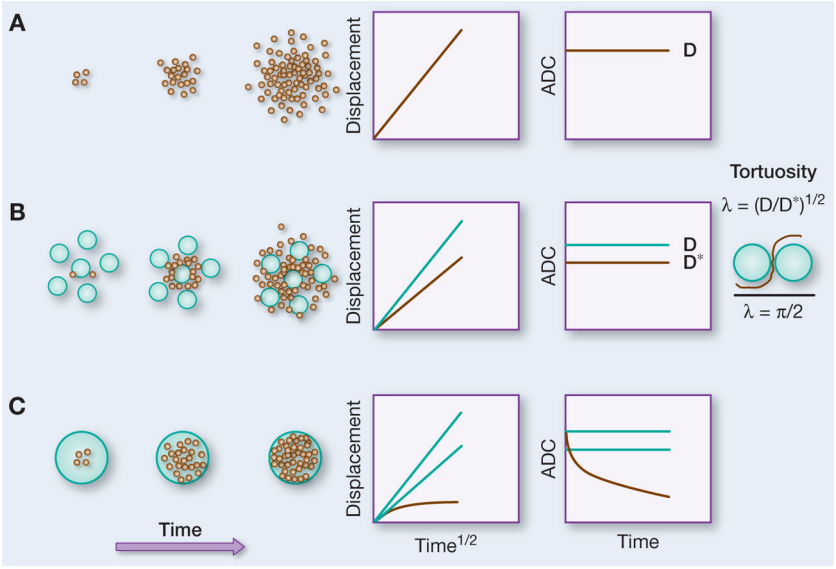

Figure 2.

The three principal modes of diffusion in tissue. (A) In free water, the average molecular excursion along a single dimension in space in terms of the root-mean-squared distance *s* increases linearly with the square root of diffusion time $s = (2DT_d)^{1/2}$ with a slope that depends on the intrinsic diffusivity *D*. (B) For hindered water in brain ECS, the net displacements remain linear with the square root of diffusion time (i.e. Gaussian) but the effective diffusion coefficient *D** (or ADC) is reduced compared with *D* due to tortuosity of the ECS. The theoretical maximum reduction in *D** (or ADC) that can be expected due to crowding of small spherical cells in the ECS is given by the tortuosity limit π/2 or 40% (35). (C) In restricted intracellular diffusion, the net distance traveled by water molecules is limited by the compartment dimensions leading to a sub-linear time evolution of the net squared displacement and a decrease ADC. The ADC of restricted intracellular water decreases with diffusion time as a larger proportion of the spins “bounce off” the plasma membrane.

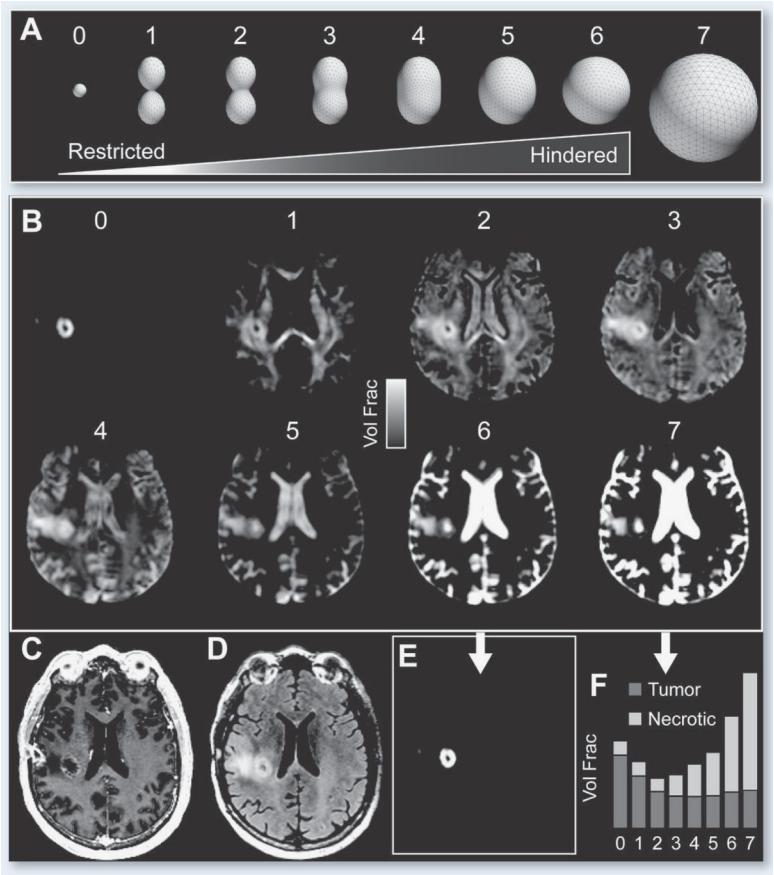

Figure 3.

RSI analysis of a 51 year-old Male with right frontal GBM. (A) Illustration of the RSI "spectrum" model used to fit the multi-b-value, multi-direction DWI data. Scales 0–2 and 3–6 correspond to restricted and hindered diffusion, respectively. Scales 0, 6, and 7 are isotropic, while Scales 1–5 are anisotropic (i.e. oriented). (B) RSI-derived (T2-weighted) volume fraction maps for each scale in A. (C) T1-weighted post-contrast (D) T2-weighted FLAIR (E) RSI-derived "cellularity map" (RSI-CM) corresponding to a weighted ("beamformed") linear combination of Scales 0–7 showing maximal sensitivity and specificity to spherically restricted diffusion (Scale 0). (F) Bar plot of volume fractions for two representative voxels in tumor and necrotic tissue, respectively.

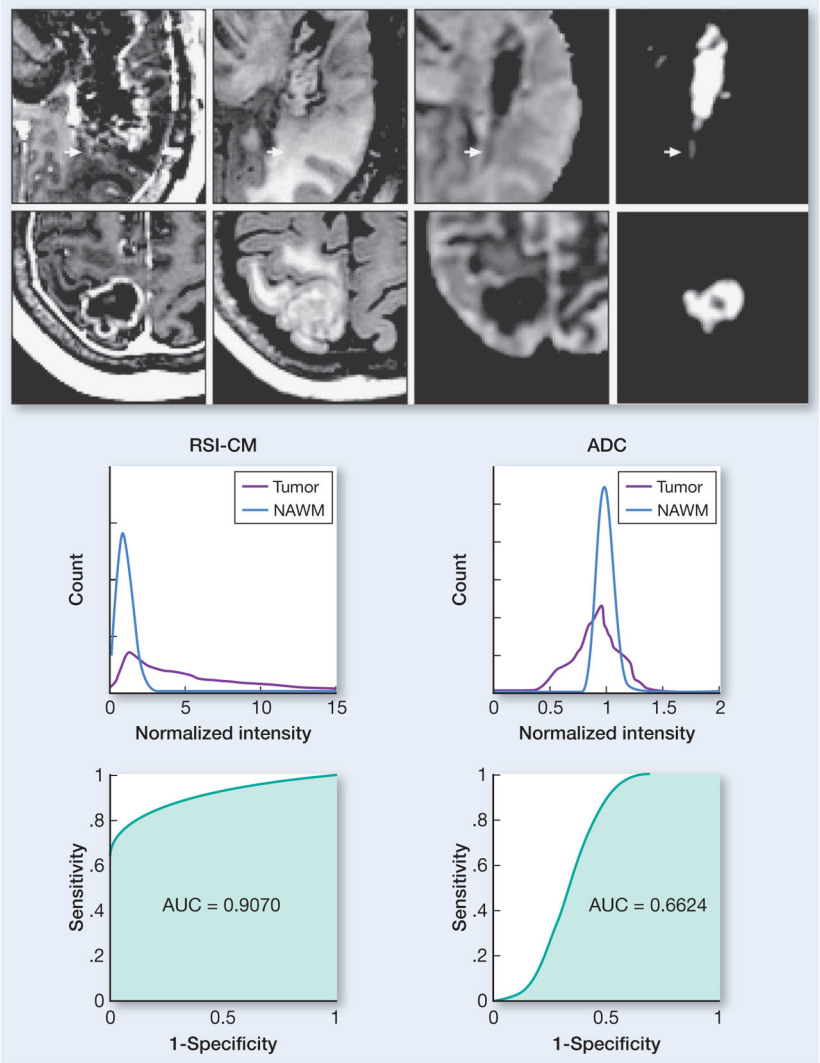

Figure 4.

From left to right: T1-weighted post-contrast, T2-weighted FLAIR, ADC, and RSI Cellularity Map for a 53 year-old male with treatment naïve right temporal GBM (top row) and a 73 year-old female with metatstatic non-small cell lung cancer. Bottom: ROC curves demonstrating increased sensitivity, specificity, and overall accuracy for delineating high grade primary and metastatic brain tumors with RSI compared with ADC. Note the high tumor conspicuity on RSI and the more protruding finger-like margins in GBM compared with metastatic disease, consistent with infiltrating tumor into peritumoral edema.

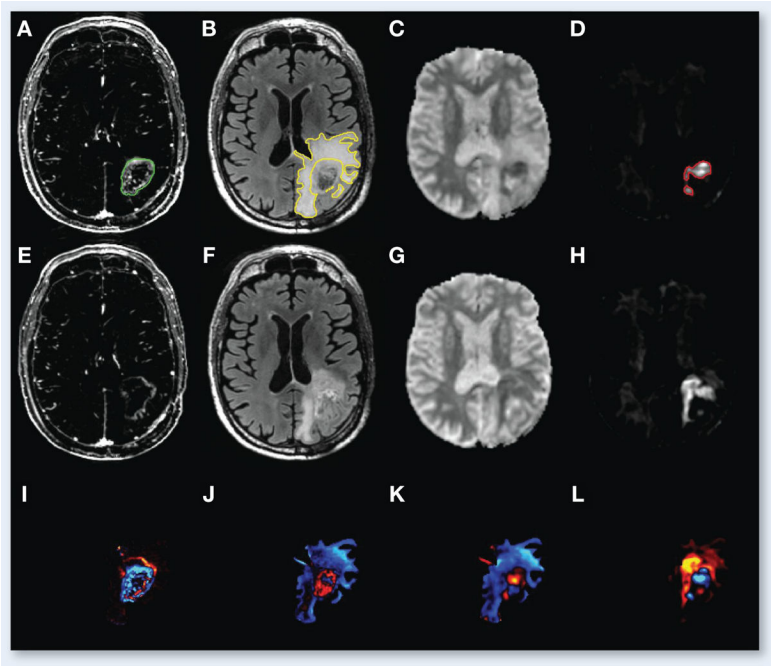

Figure 5.

67 year old male with left parietal GBM status post resection and chemoradiation. Top row shows the T1 post-contrast – T1 pre-contrast (A), FLAIR (B), ADC (C), and RSI-CMs (D) *before* the start of bevacizumab, while the middle row shows the T1 post-contrast – T1 pre-contrast (E), FLAIR (F), ADC (G), and RSI-CMs (H) *after* initiation of bevacizumab. Arrowheads point to the contrast enhancing region (green), the surrounding region of FLAIR-HI (yellow), and the region of RD on RSI-CMs (red). Although there is a decrease in contrast enhancement and surrounding FLAIR-HI after initiation of bevacizumab, the region of RD increases and become more confluent suggesting worsening residual/recurrent tumor. Moreover, this increase in the region of RD is much more conspicuous on the RSI-CMs compared to the ADC. The bottom row depicts these changes on “change maps” (change in T1 post-contrast – pre-contrast) (I), change in FLAIR (J), change in ADC (K), and change in the RSI-CMs (L) with red-yellow indicating an increase in signal intensity and blue-cyan indicating a decrease in signal intensity. Of note, on the ADC change map (K) the area of increased RD is essentially masked by the decreased signal intensity within the region of surrounding FLAIR-HI.

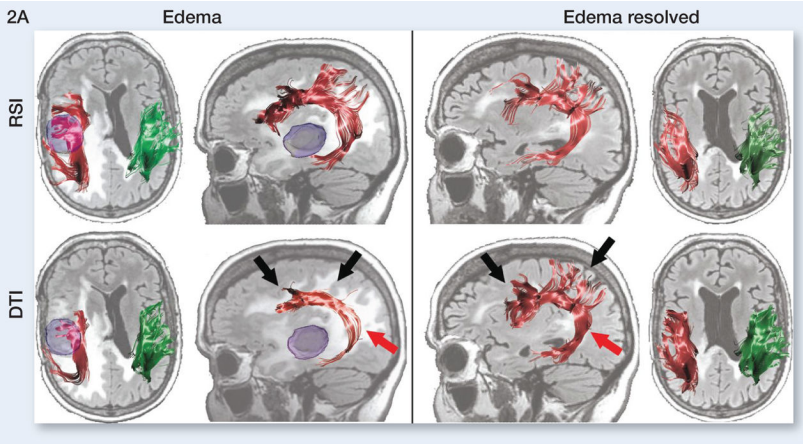

Figure 6.

Streamline tractography of the superior longitudinal fasciculus (SLF) for a 58-year old female with a right temporal lobe GBM projected onto baseline and follow-up FLAIR images. The left panel shows the RSI and DTI-based tractography at baseline in regions of edema, whereas the right panel shows data obtained using the same tractography algorithm once the edema had mostly resolved. The ipsilateral (red) and contralateral (green) 3-D renditions of the SLF are superimposed on axial and sagittal FLAIR slices collected at each time point. The GBM is shown in blue in the pre-operative image. With RSI, the SLF appears very similar at baseline and at follow-up. However, with DTI, the SLF appears thinner and truncated at baseline in regions of edema. Black arrows point to frontal and parietal regions of the SLF that terminate completely in regions of edema and the red arrow shows the sparse streamlines in the temporal portion of the SLF. These streamlines are “recovered” using DTI once the edema resolves.

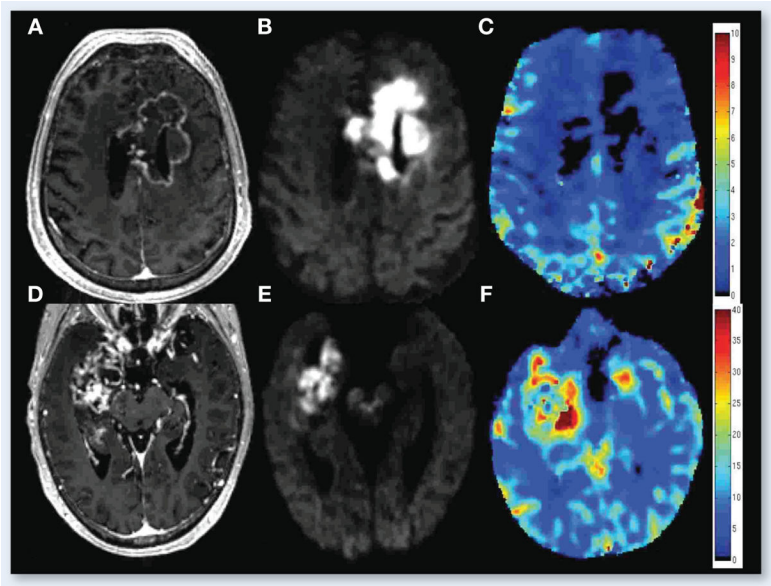

Figure 7.

Comparison of 55 year old male with GBM treated with chemoradiation and bevacizumab (top row) and 66 year old male with GBM prior to any treatment (bottom row). T1 post-contrast images (A, D), RSI maps (B, E), and rCBV maps (C, F) are shown. Degree and homogeneity of restricted diffusion is greater in the patient treated with bevacizumab than in the pre-treatment GBM control (images scaled identically with same window and level), whereas rCBV in the region of restricted diffusion is remarkably low in the patient treated with bevacizumab—lower than in the GBM control and lower than in the NAWM.

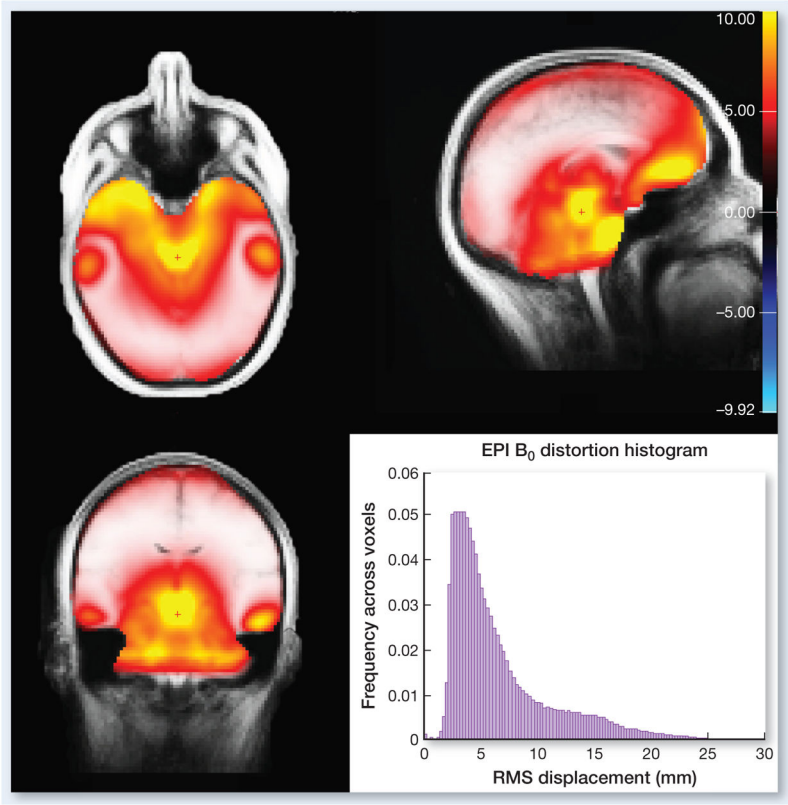

Figure 8.

3-plane map and histogram of the RMS displacement of voxels (in mm) due to B0 distortions for axially acquired EPI images (A/P phase encoding) from EPI scans of a 40 normal healthy subjects.

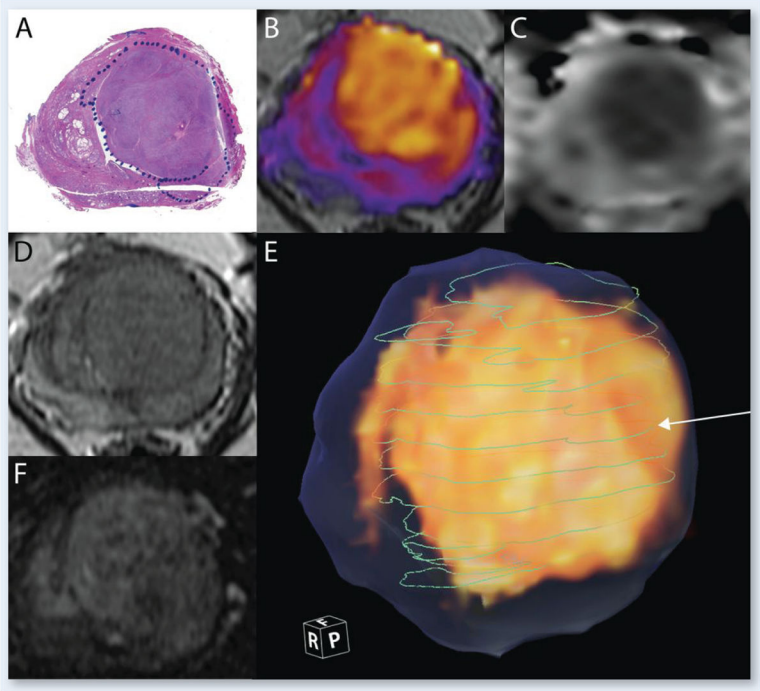

Figure 9.

Gleason 3+4. A) Histology section stained with hematoxylin and eosin. The blue dotted line indicates the boundary of the tumor B) RSI Cellularity map, color-coded and overlaid on T2; C) ADC image; D) T2 image; E) 3D volume rendering of the RSI (in yellow), the whole extent of the prostate as traced on T2 images (translucent blue), and green lines indicating the boundary of the tumor on each of the whole mount histological sections that were compared with the RSI. The white arrow indicates the line corresponding to the histology section shown in A); F) Raw perfusion data.